# Supporting Information for "High-resolution mantle flow models reveal importance of plate boundary geometry and slab pull forces on generating tectonic plate motions"

A. Saxena[1], J. Dannberg[1], R. Gassmöller[1], M. Fraters[2], T. Heister[3], and R. Styron[4]

[1]Department of Geological Sciences, University of Florida, Gainesville, FL, USA

[2]Department of Earth and Planetary Sciences, University of California, Davis, CA, USA

[3]Mathematical and Statistical Sciences, Clemson University, Clemson, SC, USA

[4]Global Earthquake Model Foundation, Pavia, Italy

**Contents of this file**



**Introduction** Our main text describes our global mantle flow model setup and presents results from our parameter study with varying plate boundary and asthenosphere viscosities and different plate boundary configurations, testing which model best fits the observed plate motions. Here we describe additional parameter variations based on our best-fit model, i.e., the model with the GEM plate geometry, an asthenosphere viscosity of $5 \times 10^{17}$ Pa s and a plate boundary viscosity of $2.5 \times 10^{20}$ Pa s.

**Influence of temperature distribution**

To account for uncertainties in lithosphere thickness, we test models with a thicker and a thinner lithosphere by shifting the TM1 temperature model (Osei Tutu et al., 2018) we use as an input upwards and downwards by 30 km, respectively. In the model with a thinner lithosphere, the plates move very fast (average rms velocity ∼14 cm/yr) compared to the average GPS velocities. This is expected because shifting the temperature structure up by 30 km leads to higher temperatures of the lithospheric mantle and consequently low-viscosity thin plates that can deform very easily. The angular fits deteriorate from 91.5% in our reference case to ≈50% in this model. Increased plate speeds in models with a thinner lithosphere were also reported by Osei Tutu et al. (2018). However, the increase in speed and angular misfit is much higher in our model due to the absence of a rigid crust in some parts of the model.

The model with a thicker lithosphere (Figure S6) has a similar angular correlation, but a higher speed residual (2.02 versus 1.25 cm/yr) and RMS residual (2.71 vs 2.05 cm/yr) compared to our reference model. The reason for this higher speed residual is an overall reduction in the speed of the plates, particularly in the oceanic plates, because the same forces are transferred to a thicker plate—an effect also observed in Osei Tutu et al. (2018)'s models. While this results in an increased speed residual for most oceanic plates (e.g., Pacific, Australia and Cocos), the reduced speed fits the observed motion of the Nazca plate better compared to the reference model, where the velocities are too high (Fig. S6, Fig. 7).

Our tests with the shifted TM1 model shows that lithospheric structure strongly affects the plate speeds and directions, and future improvements in lithospheric thickness estimates could improve the fit to the observations.

We also test a constant Vs-to-temperature anomaly scaling (Vs-to-T) factor of $-4.2$ (as in Becker, 2006) instead of the depth-dependent scaling used in our other models (from Steinberger & Calderwood, 2006). We find that our results remain largely unaffected with slightly higher velocities (average speeds are 5% more than our reference model) predicted with the constant Vs-to-T factor. This is because compared to the depth-dependent Vs-to-T values used in our other models, the constant Vs-to-T factor is larger at shallower depths (<250 km) and smaller below 250 km depth. A higher Vs-to-T scaling implies stronger temperature variations and a stronger associated buoyancy force. The increased uppermost-mantle temperature variations in the models with a constant scaling (compared to the model with depth-dependent scaling) influence the plate velocities more than the decreased lower-mantle temperature variations. The higher contribution of upper-mantle heterogeneity compared to the lower-mantle is consistent with our analysis of the forces contributing to plate motion discussed in Section 3.6 of the main text.

**Influence of grain size**

In our best-fit model, we modify the slab strength by shifting the ratio between diffusion and dislocation creep. We achieve this by reducing the grain size from 5 mm in the reference model to 1.4 mm, reducing the viscosity in regions where diffusion creep contributes to deformation. The viscosity in regions with strong deformation, such as subducted slabs, that are dominated by dislocation creep are not affected by grain size. This increases the relative viscosity contrast between subducted slabs and the rest of the

mantle. Since we scale the laterally averaged viscosity to a reference profile (see Section 2.5), changing the grain size in this way does not affect the average viscosity values, but it does lead to higher viscosities in slabs. This means that slab pull forces can now be transferred more efficiently to the plates attached to the subduction zone. Our model with reduced grain size has an improved angular correlation of 93.3% (compared to 91.5% in the reference model) and a slightly increased mean speed residual (1.4 cm/yr vs 1.25 cm/yr) with the overall effect of a marginally increased velocity residual (2.15 cm/yr from 2.05 cm/yr). In the Earth, grain size is expected to vary based on the temperature and deformation conditions, affecting the spatial variability of viscosity and therefore the mantle flow pattern (Dannberg et al., 2017). This more complex effect remains to be investigated in future studies.

## References

Argus, D. F., & Gordon, R. G. (1991). No-net-rotation model of current plate velocities incorporating plate motion model nuvel-1. *Geophysical research letters*, *18*(11), 2039–2042.

Becker, T. W. (2006). On the effect of temperature and strain-rate dependent viscosity on global mantle flow, net rotation, and plate-driving forces. *Geophysical Journal International*, *167*(2), 943–957.

Bird, P. (2003). An updated digital model of plate boundaries. *Geochemistry, Geophysics, Geosystems*, *4*(3).

Dannberg, J., Eilon, Z., Faul, U., Gassmöller, R., Moulik, P., & Myhill, R. (2017). The importance of grain size to mantle dynamics and seismological observations. *Geochemistry, Geophysics, Geosystems*, *18*(8), 3034–3061.

Osei Tutu, A., Steinberger, B., Sobolev, S. V., Rogozhina, I., & Popov, A. A. (2018). Effects of upper mantle heterogeneities on the lithospheric stress field and dynamic topography. *Solid Earth*, *9*(3), 649–668.

Simmons, N. A., Myers, S., Johannesson, G., Matzel, E., & Grand, S. (2015). Evidence for long-lived subduction of an ancient tectonic plate beneath the southern indian ocean. *Geophysical Research Letters*, *42*(21), 9270–9278.

Steinberger, B., & Calderwood, A. R. (2006). Models of large-scale viscous flow in the earth's mantle with constraints from mineral physics and surface observations. *Geophysical Journal International*, *167*(3), 1461–1481.

Styron, R., & Pagani, M. (2020). The gem global active faults database. *Earthquake Spectra*, *36*.

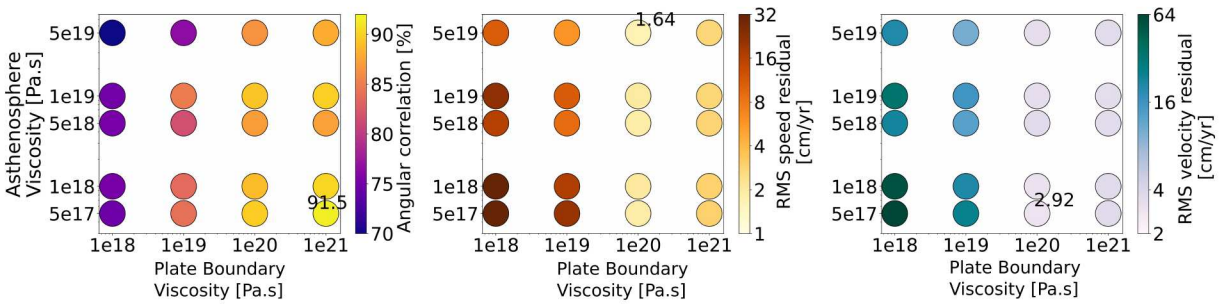


**Figure S1.** Angular correlation, mean speed residuals and velocity residuals at the surface for the models shown in Figure 4 in the main text (Bird-closed plate geometry, and using different values of plate boundary viscosity and asthenosphere viscosity). Maximum angular correlation, minimum speed residual, and minimum velocity residual are annotated in each subplot. Note that in all plots light colors represent a good fit, and saturated colors represent significant misfits.

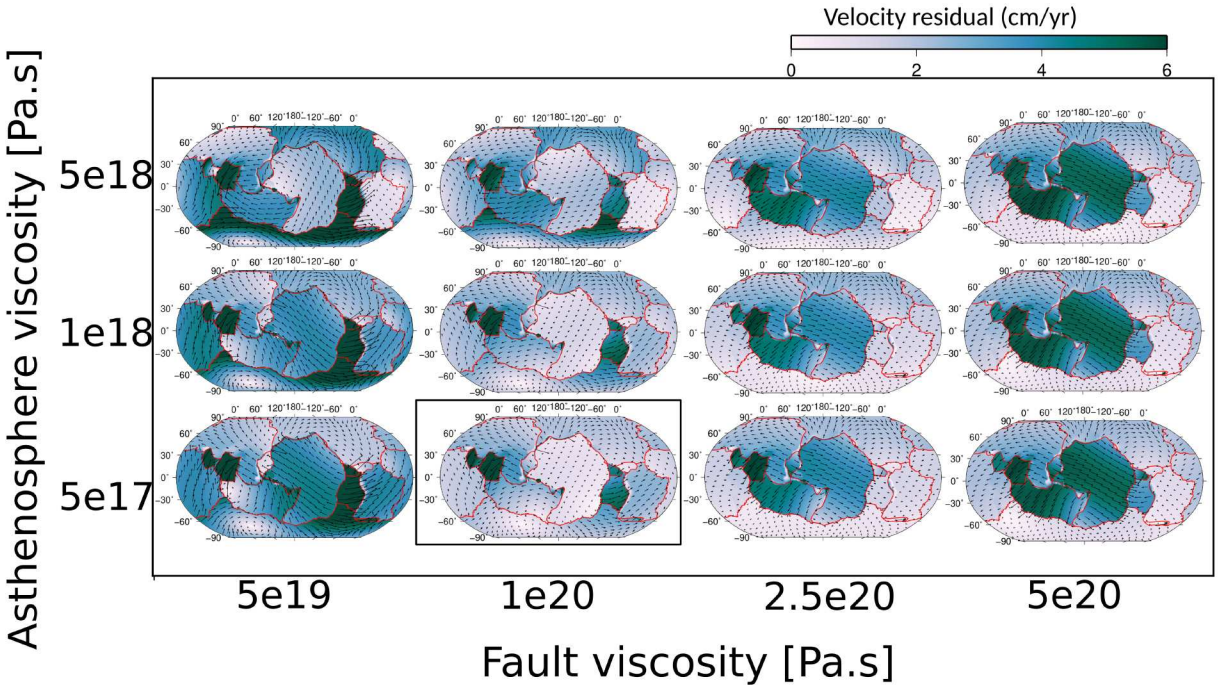


**Figure S2.** Velocity residual at the surface for different combinations of plate boundary viscosity and asthenosphere viscosity (as in Figure 5 in the main text), and using the Nuvel plate boundary geometry (Argus & Gordon, 1991). The arrows represent point-wise differences between modeled and observed velocity vectors. The black box marks the models with the lowest RMS velocity residual.

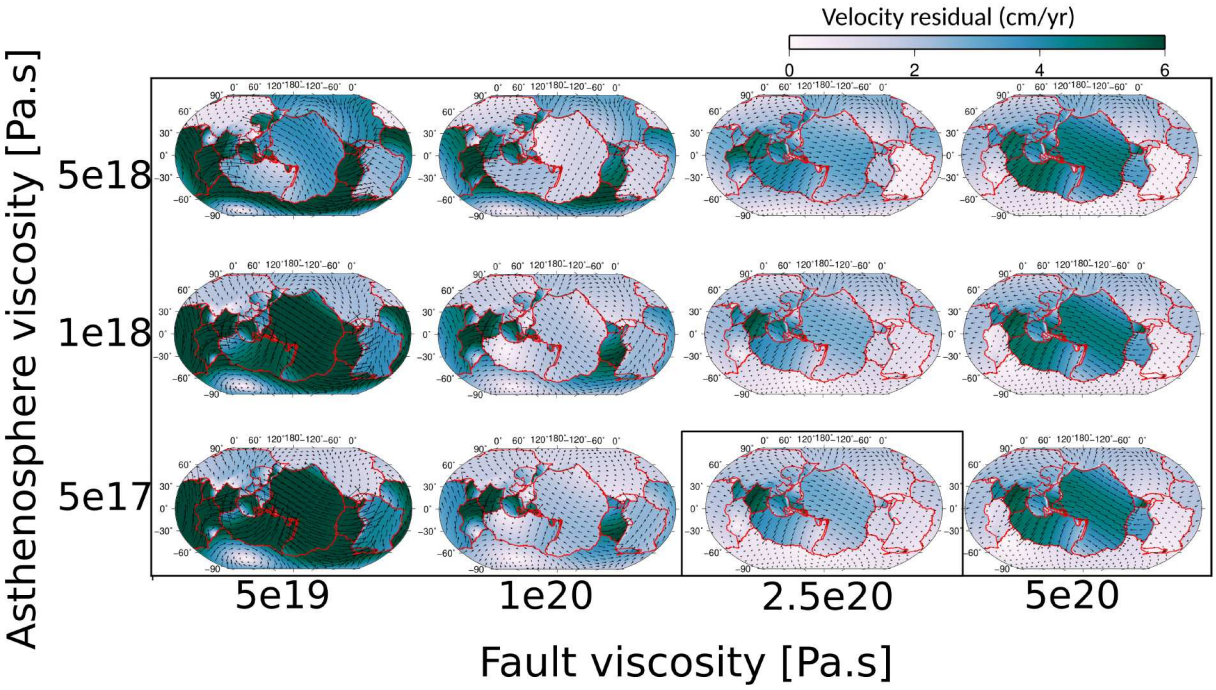


**Figure S3.** Velocity residual at the surface for different combinations of plate boundary viscosity and asthenosphere viscosity (as in Figure 5 in the main text), and using the Bird-closed plate boundary geometry (Bird, 2003). The arrows represent point-wise differences between modeled and observed velocity vectors. The black box marks the models with the lowest RMS velocity residual.

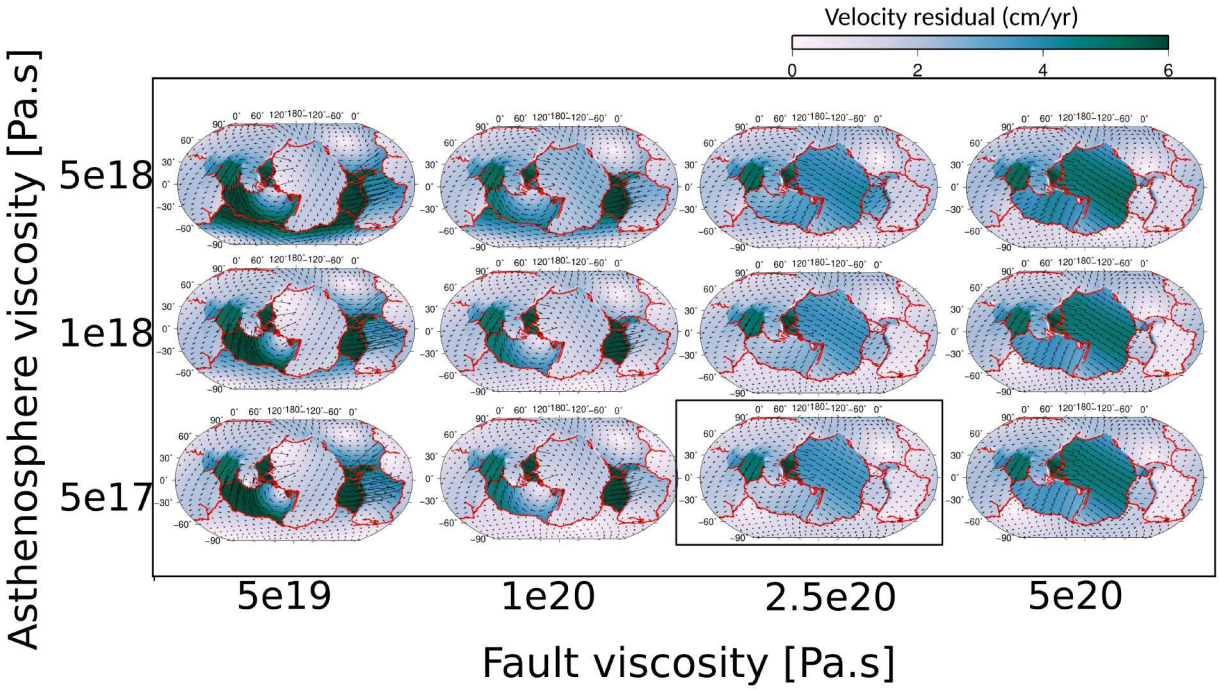


**Figure S4.** Velocity residual at the surface for different combinations of plate boundary viscosity and asthenosphere viscosity (as in Figure 5 in the main text), and using the Bird-GEM plate boundary geometry (Bird, 2003; Styron & Pagani, 2020). The arrows represent point-wise differences between modeled and observed velocity vectors. The black box marks the models with the lowest RMS velocity residual.

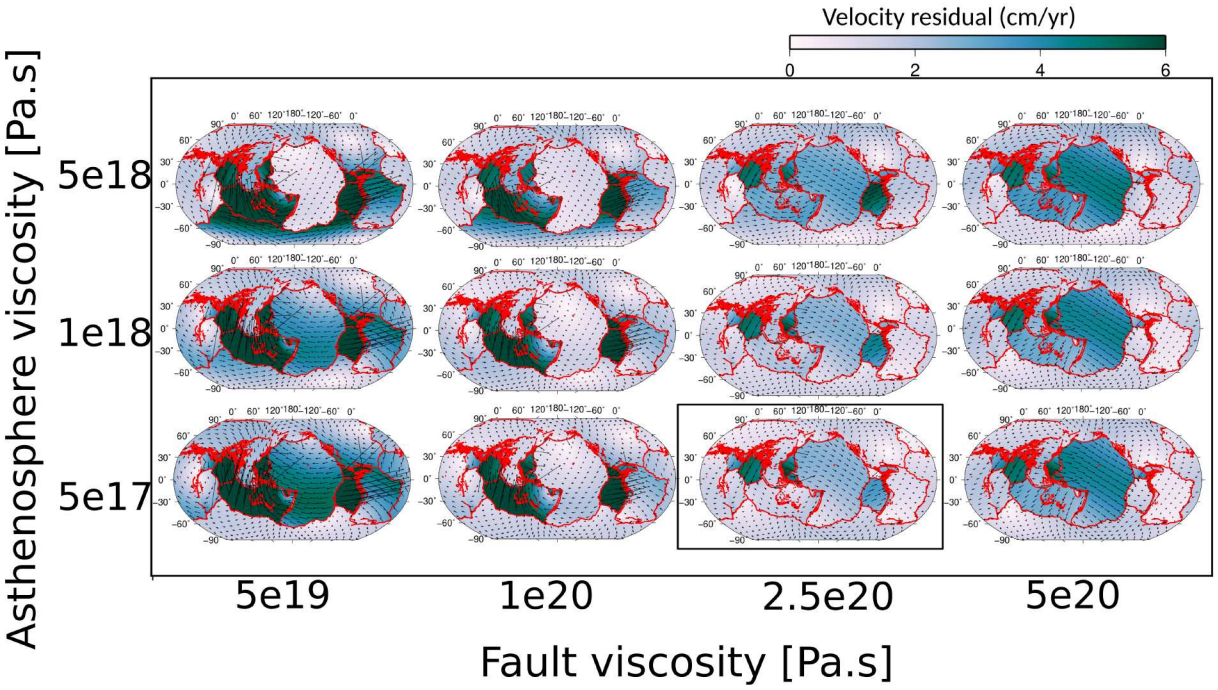


**Figure S5.** Velocity residual at the surface for different combinations of plate boundary viscosity and asthenosphere viscosity (as in Figure 5 in the main text), and using the GEM plate boundary geometry (Styron & Pagani, 2020). The arrows represent pointwise differences between modeled and observed velocity vectors. The black box marks the models with the lowest RMS velocity residual.

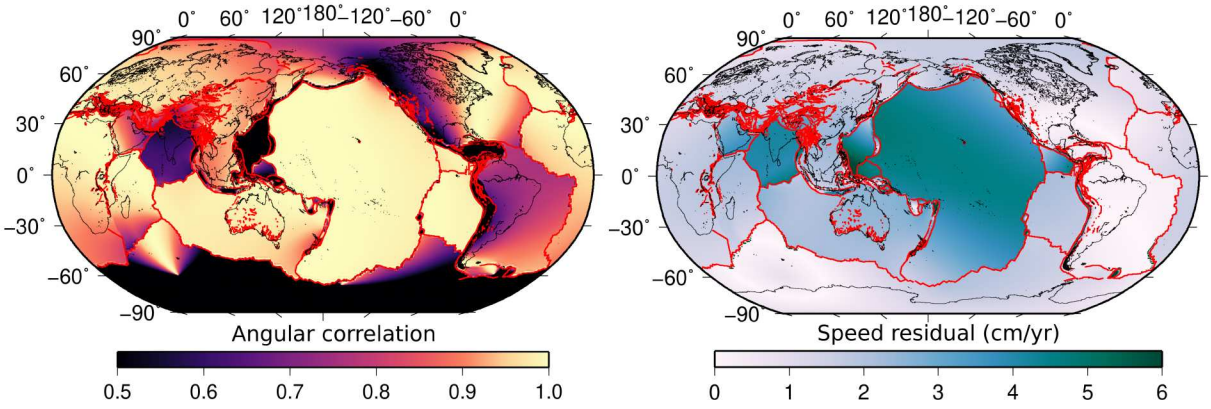


**Figure S6.** Map of angular correlation and speed residual for the model with a thicker lithosphere.

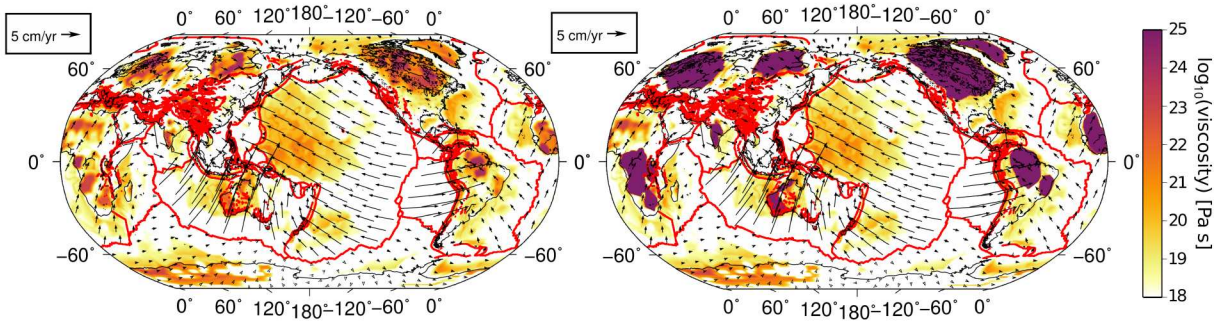


**Figure S7.** Viscosity at 100 km depth for our reference model (left) and model with stiff cratons (right). The modeled and observed surface velocities for the corresponding models are shown using black arrows, respectively.

**Table S1.** Velocity residuals of models with different transition depths between the TM1 temperature model (Osei Tutu et al., 2018) and the LLNL tomography model (Simmons et al., 2015)

| Plate boundary model | Plate boundary viscosity | Asthenosphere viscosity | TM1 to LLNL transition depth (km) | Mean velocity residual (cm/yr) |
|---|---|---|---|---|
| Bird-closed | 1e20 | 1e18 | 100 | 7.89 |
| Bird-closed | 1e20 | 1e18 | 150 | 4.71 |
| Bird-closed | 1e20 | 1e18 | 200 | 3.21 |
| Bird-closed | 1e20 | 1e18 | 300 | 3.3 |
| Bird-GEM | 1e20 | 1e18 | 150 | 3.58 |
| Bird-GEM | 1e20 | 1e18 | 200 | 3.22 |
| Bird-GEM | 1e20 | 1e18 | 300 | 3.48 |

**Table S2.** Misfit of various model configurations with varying plate boundary and asthenosphere viscosity, and plate boundary models

| Plate boundary model | Plate boundary viscosity | Asthenosphere viscosity | Angular correlation (%) | Mean speed residual (cm/yr) | Mean velocity residual (cm/yr) |
|---|---|---|---|---|---|
| Nuvel | 5e20 | 5e18 | 80.7 | 2.62 | 3.38 |
| Nuvel | 5e20 | 1e18 | 82.51 | 2.7 | 3.38 |
| Nuvel | 5e20 | 5e17 | 86.27 | 2.75 | 3.384 |
| Nuvel | 2.5e20 | 5e18 | 81.06 | 2.07 | 2.94 |
| Nuvel | 2.5e20 | 1e18 | 82.55 | 2.05 | 2.82 |
| Nuvel | 2.5e20 | 5e17 | 85.93 | 2.07 | 2.8 |
| Nuvel | 1e20 | 5e18 | 81.71 | 1.71 | 2.93 |
| Nuvel | 1e20 | 1e18 | 83.61 | 1.46 | 2.65 |
| Nuvel | 1e20 | 5e17 | 85.9 | 1.34 | 2.52 |
| Nuvel | 5e19 | 5e18 | 82.08 | 2.32 | 4.14 |
| Nuvel | 5e19 | 1e18 | 84.76 | 3 | 4.56 |
| Nuvel | 5e19 | 5e17 | 86.25 | 3.07 | 4.68 |
| Bird-closed | 5e20 | 5e18 | 87.52 | 2.33 | 3.1 |
| Bird-closed | 5e20 | 1e18 | 90.2 | 2.38 | 3.03 |
| Bird-closed | 5e20 | 5e17 | 91.21 | 2.44 | 3.05 |
| Bird-closed | 2.5e20 | 5e18 | 87.52 | 1.85 | 2.7 |
| Bird-closed | 2.5e20 | 1e18 | 89.76 | 1.67 | 2.34 |
| Bird-closed | 2.5e20 | 5e17 | 90.72 | 1.61 | 2.28 |
| Bird-closed | 1e20 | 5e18 | 87.08 | 1.91 | 3.58 |
| Bird-closed | 1e20 | 1e18 | 88.9 | 2.04 | 3.12 |
| Bird-closed | 1e20 | 5e17 | 89.78 | 1.91 | 2.92 |
| Bird-closed | 5e19 | 5e18 | 86.23 | 3.6 | 5.75 |
| Bird-closed | 5e19 | 1e18 | 88.05 | 4.7 | 6.41 |
| Bird-closed | 5e19 | 5e17 | 88.74 | 4.93 | 6.6 |
| Bird-gem | 5e20 | 5e18 | 90.4 | 2.35 | 3.01 |
| Bird-gem | 5e20 | 1e18 | 91.68 | 2.32 | 2.9 |
| Bird-gem | 5e20 | 5e17 | 91.87 | 2.31 | 2.87 |
| Bird-gem | 2.5e20 | 5e18 | 89.4 | 2.06 | 2.73 |
| Bird-gem | 2.5e20 | 1e18 | 90.88 | 1.8 | 2.44 |
| Bird-gem | 2.5e20 | 5e17 | 91.21 | 1.74 | 2.37 |
| Bird-gem | 1e20 | 5e18 | 87.34 | 2.25 | 3.48 |
| Bird-gem | 1e20 | 1e18 | 89.82 | 1.85 | 3.22 |
| Bird-gem | 1e20 | 5e17 | 89.4 | 1.71 | 3.06 |
| Bird-gem | 5e19 | 5e18 | 85.5 | 2.81 | 5.13 |
| Bird-gem | 5e19 | 1e18 | 86.6 | 2.7 | 5.67 |
| Bird-gem | 5e19 | 5e17 | 86.9 | 2.61 | 5.64 |
| GEM | 5e20 | 5e18 | 90.88 | 2.04 | 2.77 |
| GEM | 5e20 | 1e18 | 93.01 | 2 | 2.61 |
| GEM | 5e20 | 5e17 | 92.67 | 2.01 | 2.6 |
| GEM | 2.5e20 | 5e18 | 90.06 | 1.65 | 2.56 |
| GEM | 2.5e20 | 1e18 | 92.1 | 1.33 | 2.15 |
| GEM | 2.5e20 | 5e17 | 91.5 | 1.25 | 2.05 |
| GEM | 1e20 | 5e18 | 88.15 | 1.96 | 3.96 |
| GEM | 1e20 | 1e18 | 89.92 | 1.79 | 4.05 |
| GEM | 1e20 | 5e17 | 89.24 | 1.87 | 4 |
| GEM | 5e19 | 5e18 | 86.32 | 2.85 | 6.12 |
| GEM | 5e19 | 1e18 | 87.57 | 3.83 | 7.66 |
| GEM | 5e19 | 5e17 | 87 | 4.21 | 8 |